frontiers | Frontiers in Physics

TYPE Original Research
PUBLISHED 31 October 2024
DOI 10.3389/fphy.2024.1503269

OPEN ACCESS

EDITED BY
Yaping Dan,
Shanghai Jiao Tong University, China

REVIEWED BY
Massimo Cazzanelli,
University of Trento, Italy
Jiajing He,
Chinese Academy of Sciences (CAS), China

*CORRESPONDENCE
Pengzhan Zhang,
pzzhang@jit.edu.cn

RECEIVED 28 September 2024
ACCEPTED 23 October 2024
PUBLISHED 31 October 2024

CITATION
Zhang P, Liu X, Zhang L, Wang D, Wu K and Wang S (2024) Temperature dependent radiative and non-radiative recombination lifetimes of luminescent amorphous silicon oxynitride systems.
Front. Phys. 12:1503269.
doi: 10.3389/fphy.2024.1503269

Temperature dependent radiative and non-radiative recombination lifetimes of luminescent amorphous silicon oxynitride systems

Pengzhan Zhang[1,2]*, Xinyu Liu[1], Ling Zhang[1], Danbei Wang[1], Kongpin Wu[1] and Sake Wang[1]

[1]College of Electronic and Information Engineering, Jinling Institute of Technology, Nanjing, China, [2]Collaborative Innovation Center of Advanced Microstructures, National Laboratory of Solid-State Microstructures, Nanjing University, Nanjing, China

In our previous work, we deeply researched the absolute photoluminescence (PL) quantum yields of luminescent modulating a-SiN_xO_y films with various N/Si atom ratios under different measurement temperatures. In this work, we further systematically studied the temperature dependent kinetic processes of radiative and non-radiative recombinations in a-SiN_xO_y systems in the visible light range. First, we investigated the structure of a-SiN_xO_y films and obtained the concentrations of both trivalent Si and N-Si-O defects related dangling bonds through XPS, FTIR and EPR measurements. Then we further tested the transient fluorescence attenuation of a-SiN_xO_y films detected at different emission wavelengths. We found that the PL lifetimes of a-SiN_xO_y films vary with the change of N-Si-O defect state concentrations, which is different from the typical PL decay characteristics of band tail related a-SiN_x films previously reported. By combining the resulting PL IQE values with the ns-PL lifetimes, we further intensively redetermined the radiative and non-radiative recombination lifetimes of a-SiN_xO_y systems. The related radiative recombination rates were obtained (k_r~10^8 s^{-1}), which can be compared to the results in the direct band gap.

KEYWORDS

a-SiN_xO_y, PL lifetimes, defect states, radiative recombination rates, non-radiative recombination lifetimes

1 Introduction

To realize Si-based monolithic photoelectric integration, the most critical task of various components in the related integration manufacturing processes is to realize Si-based light sources with highly efficient luminescence. However, due to the indirect band gap of Si, the related luminescent efficiencies are very low. Therefore, based on improving the absolute photoluminescence quantum yields (PL AQYs) and PL internal quantum efficiencies (PL IQE), the study of the PL properties and the related dynamics processes in Si-based high-efficient luminescent

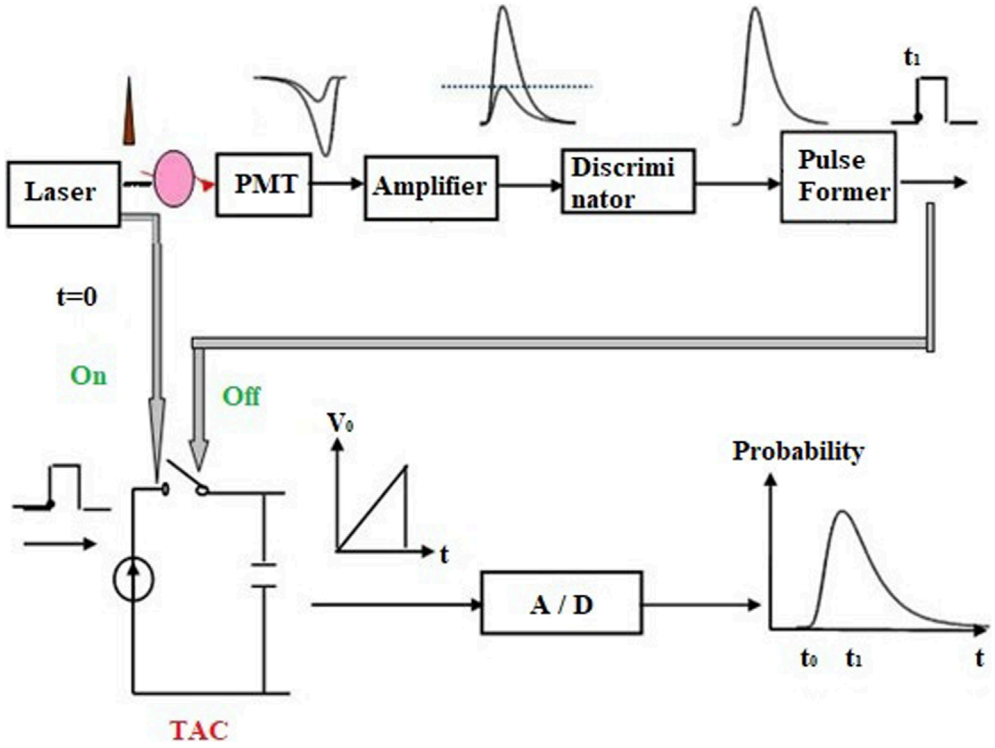

FIGURE 1
A diagrammatic presentation of the principle of TCSPC measurement methods.

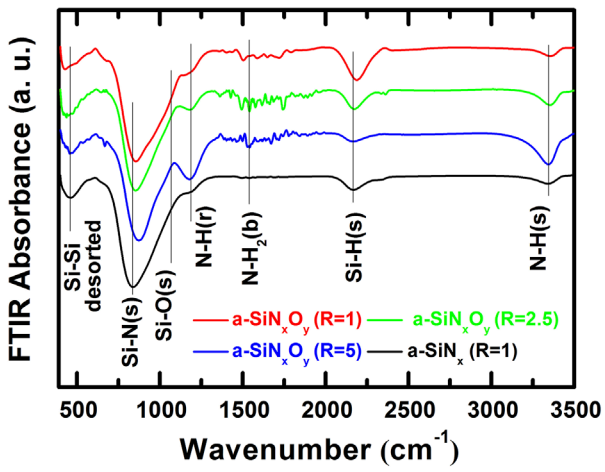

FIGURE 2
FTIR spectra of a-SiN_xO_y films with different N/Si ratios and the controlled a-SiN_x films.

materials has become one of the research hotspots for more than 2 decades [1, 2].

Most of the previous researches on the luminescence mechanisms and the related PL decay processes has focused on Si nanostructured materials, such as porous silicon (PS Si) [3, 4], colloidally passivated Si quantum dots [5–9], and nc-Si embedded Si-based films [10–15]. Only a few reports were talked about Si-based compounds, such as amorphous silicon carbide (a-SiC_x) [16, 17], amorphous silicon nitride (a-SiN_x) [18, 19], and amorphous silicon nitride oxide (a-SiO_xN_y) [20–25]. And they found that the PL lifetimes of a-SiN_x and a-SiO_xN_y films are generally in the nanosecond range [15–18, 20]. Yang's group studied the luminescence characteristics of a-SiNx films with tail states under different components and found that PL lifetime is related to luminescence peak position (E_{PL}) [18]. Kato et al. studied in detail that the PL dynamics of a-SiN_x and a-SiO_xN_y with tailed luminescence and found that the fluorescence decay time scale is in the range of 10^{-8} to 10^{-4} s. The E_{PL} of transient fluorescence spectra changes over time in the nanosecond (~100 ns) to microsecond time scales [20].

In the previous work, we deeply researched the absolute PL quantum yield of light-emitting modulating a-SiO_xN_y films in the visible range under different test temperatures, and briefly analyzed their luminescence origins [23]. In this paper, we combined temperature dependent PL (TD PL) and time-resolved PL (TR PL) spectroscopy to further systematically study the kinetic processes of radiation recombination and non-radiative recombination processes of a-SiN_xO_y films with various N/Si atom ratios under different test temperatures. First, we investigated the structure of the a-SiN_xO_y films through XPS and FTIR measurements, and obtained the concentrations of both silicon and N-Si-O defects related dangling bonds by EPR measurements. Then, we studied the transient fluorescence properties at different detection wavelengths, and found that the luminescence lifetimes of

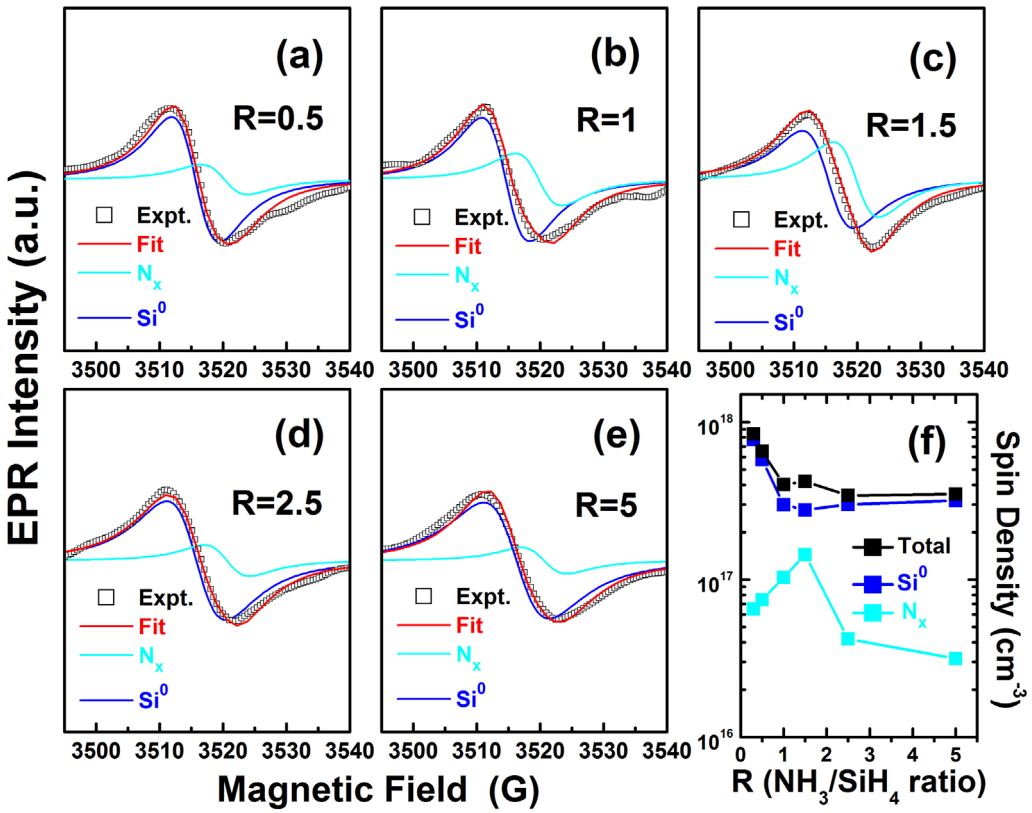

FIGURE 3
The measured EPR and the related deconvolved signals of the a-SiN_xO_y films with **(A)** R = 0.5; **(B)** R = 1; **(C)** R = 1.5; **(D)** R = 2.5; **(E)** R = 5. **(F)** The spin densities of total defects, Si DBs, and N_x defects vs R.

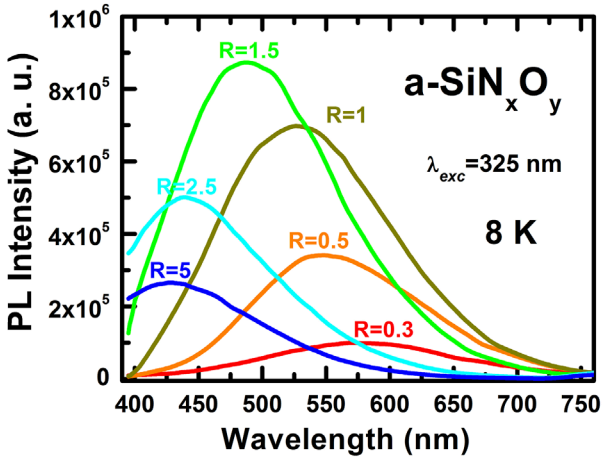

FIGURE 4
PL spectra of a-SiN_xO_y films with different R at 8 K under 325 nm He-Cd laser excitation.

samples changed with the variation tendency of the concentrations of N-Si-O defect states, which was different from the typical band tail luminescence kinetic characteristics reported in the past. Furthermore, we tested the PL lifetimes of a-SiO_xN_y films at different temperatures, and analyzed the related radiative and non-radiative recombination processes. Based on the measured PL lifetimes of the a-SiO_xN_y films at different temperature range, combined with the PL IQE values obtained earlier, we calculated the radiative and non-radiative recombination lifetimes of a-SiO_xN_y films at different temperatures. At last, we deeply analyzed the change law between the radiative recombination processes of a-SiO_xN_y films and the concentration of N-Si-O defect states. We found that the radiation recombination rates of the films are almost unchanged over the whole temperature range. The obtained radiative recombination rates kr~10^8 s^{-1} can be compared with the results in the direct band gap (such as CdSe nanocrystals).

2 Materials and methods

2.1 Material fabrication

The a-SiN_xO_y films (~500 nm) were deposited on polished Si substrates in a plasma-enhanced chemical vapor deposition (PECVD, OXFORD Plasmalab 80PLus, Oxford, UK) system with a silane, ammonia, and nitrogen gas mixture The gas flow ratios R (R = NH_3/SiH_4) and the related fabrication parameters were well controlled through the whole fabrication processes, both of which were described in our previous work last year in detail [23]. After

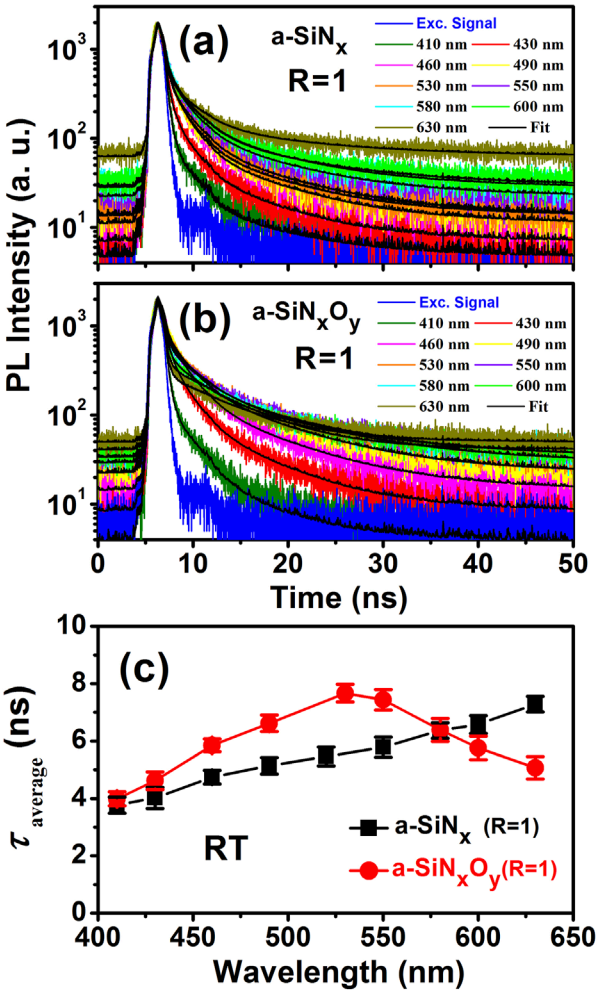

FIGURE 5
The excitation signal (blue line), the measured ns-TR PL decay spectra and the relative fitted decay curves (black line) of both **(A)** a-SiN_x films (R = 1) and **(B)** the controlled a-SiN_xO_y films detected at different emission wavelengths (λ_{emi}). **(C)** The ns-PL lifetimes $\tau_{average}$ vs λ_{emi} for a-SiN_xO_y samples (R = 1) and the controlled a-SiN_x films at RT. Red and black lines show the error bars of the ns-PL lifetimes $\tau_{average}$.

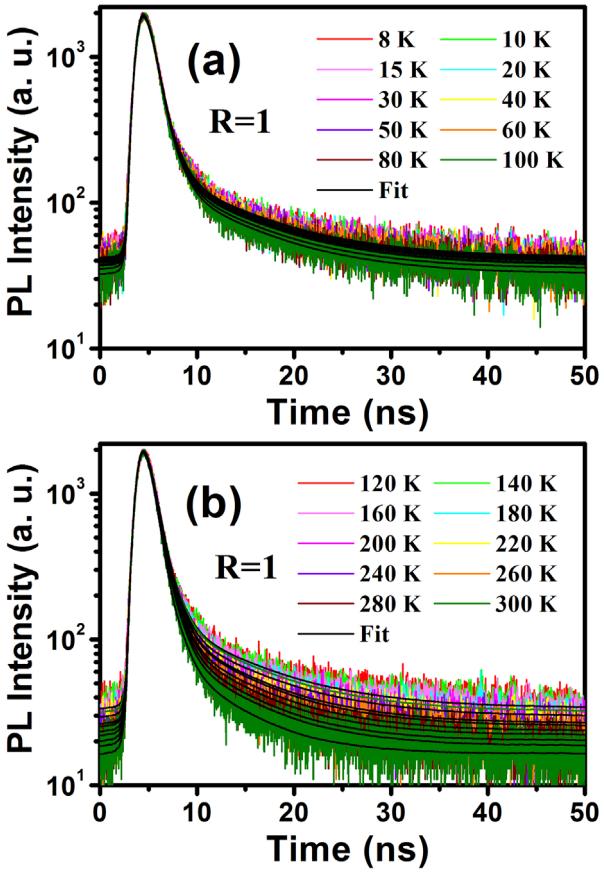

FIGURE 6
The measured ns-TRPL decay spectra and the relative fitted decay curves (black line) for a-SiN_xO_y samples with R = 1 under measurement temperature range of **(A)** from 8 K to 100 K, **(B)** from 120 K to 300 K, respectively.

fabrication, the samples were subsequently oxidized *in situ*, and then post-treated by combining thermal annealing with pulsed laser annealing.

2.2 Characterization of A-SiN_xO_y thin films

The structure of the a-SiN_xO_y films was investigated through XPS and FTIR measurements. To intensively investigate the atom scale structure defects of a-SiN_xO_y thin films, we measured the EPR spectra under different R conditions at room temperature with a Bruker EMXplus in the X-band (microwave frequency f~9.85 GHz, microwave power 20 mW). The temperature dependent time resolved PL (TD-TRPL) properties of a-SiN_xO_y films with different R were measured with a Fluorolo-3 system (Jobin Yvon) and a HP4284 LCR meter in a computer-controlled Delta 9,023 oven, using a FLS980 (Edinburgh Instrument) equipped with an EPL375 pulse diode laser (pulse width ~53 ps, repetition rate = 20 MHz, λ_{exc} = 375 nm, pumping fluence W_{PF} = 5 mJ/cm^2) as light sources. A time-correlated single photo counting (TCSPC) system (time resolution ~100 ps) were used to record the characteristics of TD-TRPL decay properties. Here we consider that the initial decay of the PL intensity coincides with the excitation signal which is origin from the instrumental response (the instrumental response is about 100 ps). Thus, to deduct the impact of the initial excitation signal, we carefully deconvolved the measured ns-PL decay curves and modified the $\tau_{average}$.

2.3 Time-correlated single photo counting (TCSPC) measurement methods

The principle of TCSPC is shown in Figure 1, where a sample is first excited with a narrow laser pulse, and the sample emits fluorescent photons after stimulus. It is assumed that the excitation laser pulse is weak enough so that the sample produces only a single fluorescent photon after each pulse. The time it takes for the first fluorescent photon emitted by the sample to reach the optical receiver (which can also be seen as the time *t* when a

single photon appears) is then measured. This time is proportionally converted into a corresponding voltage pulse by TAC, which is then fed into a multichannel analyzer via A/D conversion. Multiple counts are then performed, and in the multi-channel analyzer, these output pulses are sequentially fed into each channel for cumulative storage. Since the probability of a photon being detected in a certain time interval is proportional to the intensity of the fluorescence emission, repeated measurements can obtain a P(t) histogram of the probability distribution of fluorescent photons that is essentially the same as the original waveform. The histogram measured in this case is equivalent to the I(t) curve of the decay of fluorescence intensity over time after excitation has stopped. This is as if a beam of light (many photons) passing through a small hole creates the same diffraction pattern as a single photon passing through a small hole over a long period of time.

2.4 The PL lifetimes fitting methods of a-SiN_xO_y films

In general, the PL of solid films is a non-equilibrium radiation process, and the luminescence can continue for a period (>10^{-11} s) after the excitation stops. When the excitation stops, the PL intensity I(t) decays exponentially over time. The time required when I(t) drops to 1/e of the maximum intensity at excitation is called PL lifetimes (τ) of the excited state, which indicates the average time that a particle exists in the excited state. $\tau_{average}$ at a specific temperature can be generally obtained according to the formula $I(t) = I_0\, exp(-t/\tau(T))$ [1]. The PL lifetimes of luminescent materials are related to their own structure, and this phenomenon mostly occurs from the nanosecond to the microsecond time range, which is in the time scale of molecular movement. Therefore, the property changes of the systems and the intermolecular interaction processes can be directly understood by the PL lifetimes determination. In particular, when fitting fast fluorescence lifetimes, two major types of fitting may be used: tail fitting and reconvolution fitting.

The stretched exponentials are used widely and accepted as good markers of light recombination in disordered systems [16, 18, 20]. For comparison, we firstly checked the recombination processes in the controlled a-SiN_x films by using stretched exponential model and obtained nice fitting results. However, in the fitting processes of a-SiN_xO_y systems, we found that if we use stretched exponential model, the error is large and the fitting results are unstable. For band tail related a-SiN_x films, the excited carriers relax to the deeper tail states then through the thermalization and radiative recombination to give luminescence. With the increasing excitation photon energy (E_{exc}), the excited carriers occupied the higher states in the band tail [18]. In our a-SiN_xO_y systems, we have confirmed that the light emission is mainly originated from the N-Si-O-related defect centers in our previous work [21, 23]. The defect luminescence model has been confirmed by the Stokes Shift between Urbach edge ($E_{U\,Edge}$) and PL energy (E_{PL}) $\left(\Delta E_{stokes} = E_{U\,Edge} - E_{PL}\right)$ from PLE measurements. We found that the E_{PL} Stokes Shift showed a near constant value of about 0.75 eV, which were independent on the optical band gap. There are two steps in the PL recombination process of a-SiN_xO_y films. Firstly, the excited electronics are relaxed down to the band tail states meanwhile thermally ionized to the defect states in the band gap through non-radiative processes, then recombine via transition between the defect states and valence band tail states to give luminescence [21]. The recombination processes of a-SiN_xO_y films are different from band tail related a-SiN_x films. Thus, here we choose the double exponential decays [11] instead of stretched exponentials to fit the PL lifetimes of a-SiN_xO_y films.

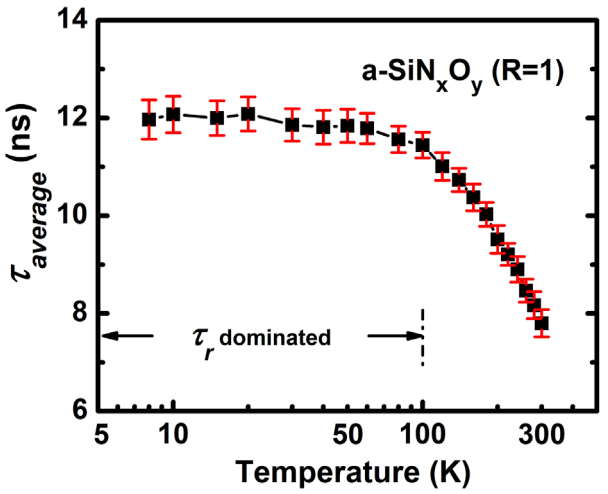

FIGURE 7
The obtained ns-PL lifetimes $\tau_{average}$ for a-SiN_xO_y samples with R = 1 vs measurement temperatures. Red lines show the error bars of the ns-PL lifetimes $\tau_{average}$ values.

3 Results and discussion

3.1 Chemical composition and bonding configurations

The presence of Si, N, and O is measured from the binding energies of the Si 2p, N 1s, and O 1 s peaks in the XPS spectrum [23]. After the top layer (~60 nm) was removed by Ar ion beam, the O concentration changed slightly, and the average oxygen content in a-SiN_xO_y films for different R was about 3.5%. As the sputtering time increases, the O concentration tends to stabilize, which is direct evidence of the incorporation of O into a-SiN_x. In order to further verify the N-Si-O bonding configuration, we measured the Fourier infrared absorption spectra (FTIR) of a-SiN_xO_y films and the corresponding a-SiN_x films.

As shown in Figure 2, the vibration peaks of the Si-Si disordered structure (460 cm^{-1}), the Si-N stretching mode (840 cm^{-1}), the N-H rocking mode (1,170 cm^{-1}), the Si–H stretching mode (2,150 cm^{-1}), and the N–H stretching mode (3,350 cm^{-1}) are clearly visible in both of a-SiN_xO_y films and the controlled a-SiN_x films. However, the Si-O stretch mode (1,070 cm^{-1}) was not seen in all FTIR spectra, suggesting that the oxygen atoms were incorporated only as trace impurities. It is worth noting that, from the vibration peaks of the Si-N stretching mode, we found that the Si-N stretching peaks of a-SiN_xO_y films are slightly shifted to the direction of higher wavenumbers than those of a-SiN_x, and there is already an obvious shoulder peak (such as R = 1). This shoulder is clearly derived

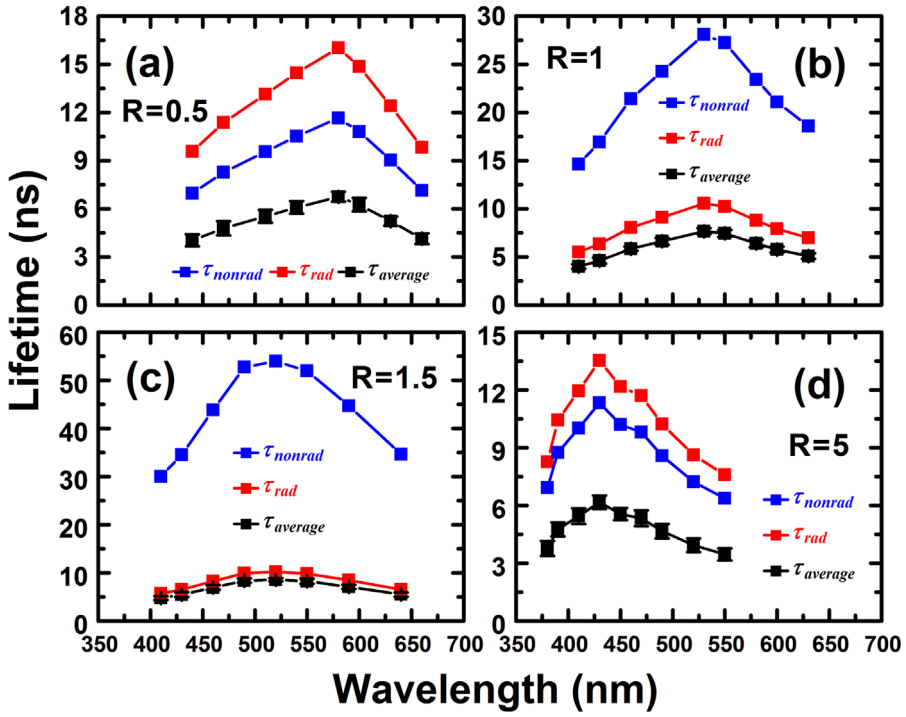

FIGURE 8
The ns-PL lifetimes $\tau_{average}$, and the calculated τ_r and τ_{nr}, vs λ_{emi} for a-SiN_xO_y with various R of **(A)** R = 0.5; **(B)** R = 1; **(C)** R = 1.5; **(D)** R = 2.5; under room temperature, respectively. Black lines show the error bars of the ns-PL lifetimes $\tau_{average}$ values.

from the N-Si-O bonding configuration formed in a-SiN_x by the incorporation of O.

3.2 N-Si-O related N_x dangling bond defect states

Figure 3 shows the measurements of the EPR curves of a-SiN_xO_y films with different R. As can be seen from Figure 3, there is a strong resonance absorption peak near the *x*-axis with magnetic induction intensity of 3,515 G, indicating the presence of unpaired dangling bonds in a-SiN_xO_y films. Since the structure of a-SiN_xO_y films is regarded as an intermediate state with both a-SiN_x and a-SiO_x, it has been found that the suspensory bond defect states in the bandgap of a-SiN_x and a-SiO_x films may coexist in a-SiN_xO_y films. We calculated the value range of the zero-crossing g-factor under different R of a-SiN_xO_y films is 2.0025–2.0040, and the peak line width is 8.5–12.0 Gauss.

According to previous analysis [21], we selected the trivalent Si DBs and the N-Si-O configurations related N_x defect states, and performed Lorentz function fitting on the experimental EPR curves. The fitting results show that the trivalent Si DBs and N_x defect states coexist in the band gap of the a-SiN_xO_y film, and the relative dangling bond concentrations of the two defect centers are also obtained by fitting. Combined with the PL spectra of a-SiN_xO_y films of different R [23], we found that the PL integrated intensities (I_{PL}) of a-SiN_xO_y films were proportional to the concentrations of N-Si-O related N_x dangling bond defect states. At the same time, we also found that the relative concentration of Si DBs in a-SiN_xO_y films was much higher than that in the N_x defect states. However, due to the low PL efficiency of Si DBs defects in a-SiN_xO_y thin films [20], they can even be regarded as non-radiative recombination centers.

3.3 Fluorescence properties of a-SiN_xO_y films

We measured the PL spectra of a-SiN_xO_y films with different R ratios at 8 K under He-Cd continuous laser excitation at a wavelength of 325 nm. As shown in Figure 4, by adjusting the flow ratio R, we achieved a fluorescence emission of a-SiN_xO_y films with modulated luminescence wavelengths (λ_{PL}) in the visible range. It is worth noting that as R increases from 0.3 to 5, the PL peak blue shifts from 590 nm to 425 nm as R gradually increases; the corresponding PL integrated intensity (I_{PL}) first increases and reaches saturation (R = 1.5), and then gradually decreases.

3.4 TR PL decay properties of a-SiN_xO_y thin films

To further investigate the relationship between the PL properties of a-SiN_xO_y films and the defect states of N-Si-O-related N_x dangling bonds, we systematically measured the ns-transient fluorescence PL characteristics of a-SiN_xO_y films (R = 1) at different

TABLE 1 Summary of the calculated τ_r, τ_{nr}, k_r and k_{nr} by using the PL IQE (η) and the obtained lifetimes $\tau_{average}$ under room temperature for a-SiN_xO_y films with various R.

	R (R = NH_3/SiH_4) ratios					
	5	2.5	1.5	1	0.5	0.3
η (%)	45.6	56.9	84.1	72.7	42.1	34.5
$\tau_{average}$ (ns)	6.17	6.92	8.57	7.66	6.75	5.64
τ_r (ns)	13.52	12.16	10.19	10.54	16.03	16.35
τ_{nr} (ns)	11.33	16.05	53.92	28.08	10.16	8.61
k_r (10^8 s^{-1})	0.74	0.82	0.98	0.95	0.62	0.61
k_{nr} (10^8 s^{-1})	0.88	0.62	0.19	0.36	0.98	1.16

detection wavelengths. As a comparison reference, we also measured the related properties of a-SiN_x films with the same flow ratio.

Figures 5A, B show the ns-TRPL decay spectra and the relative fitting decay curves for a-SiN_x and a-SiN_xO_y thin films at R = 1, respectively. According to the formula $I(t) = A_1\,exp(-t/\tau_1) + A_2\,exp(-t/\tau_2)$ with $\tau(T) = \sum_{i=1}^{n} \frac{A_i\tau_i^2}{A_i\tau_i}$ [11], we obtain the corresponding ns-PL lifetimes ($\tau_{average}$) at different detection wavelengths, as shown in Figure 5C.

From Figure 5C, we can see that for a-SiN_x films, the PL lifetimes of the samples continue to increase as the detection wavelength increases. This is a typical radiative recombination dynamics process of the band tail carrier transition, which is consistent with the previously reported results [18]. When the excitation photon energy (E_{exc}) is less than the optical band gap (E_{opt}) ($E_{exc} < E_{opt}$), the absorption only occurs at the band tail, and with the decrease of E_{exc}, the luminescence peak E_{PL} gradually shifts to the deeper energy level of the band tail, that is, the E_{PL} red shift. At this time, the excited state carriers relax to the deeper energy level of the band tail, and emit light through thermal ionization inter-band recombination, resulting in a longer corresponding PL lifetime.

However, for a-SiN_xO_y films, with the increasing detection wavelength, the fluorescence lifetime of the sample first increases to saturation, and then gradually decreases, and its change trend is obviously different from that of a-SiN_x films, but consistent with the change trend of defect density distribution, and the corresponding fluorescence lifetime value is proportional to the concentration of N_x defect states. Therefore, we believe that the N_x luminescence defect states related to the N-Si-O configuration dominate the radiation recombination process of a-SiN_xO_y films. The ns-TRPL properties of the a-SiN_xO_y films mentioned above verify that our high-efficiency light emission originates from the N-Si-O-related defect luminescence centers of the ns-order radiative recombination processes.

3.5 Temperature dependent ns-PL lifetimes of a-SiN_xO_y films

Next, to gain a deeper understanding of the radiative and non-radiative recombination mechanisms of high-efficient light emission from N-Si-O-related defect luminescence centers, we studied the PL kinetics of a-SiN_xO_y films at different test temperatures. Figure 6 shows the PL decay curve for the ns time range of a-SiN_xO_y thin films (R = 1) at a measured temperature range of 8 K–300 K. As shown in Figure 6A, the PL decay curve profiles remain unchanged at the test temperature range below 100 K, indicating that radiative recombination dominates the entire recombination process. When the test temperature is increased from 120 K to 300 K, it can be seen from the PL decay curve that the PL lifetimes of a-SiN_xO_y films become shorter, and the non-radiative recombination effects become more and more obvious, as shown in Figure 6B.

At the same time, from the PL decay curve of a-SiN_xO_y films, we can further see two different ns fluorescence radiation recombination processes, which we call the fast ns-PL lifetimes and the slow ns-PL lifetimes, respectively. The PL decay curves of a-SiN_xO_y films were well fitted with a double exponential function, and the fitting results for all PL lifetimes are shown in Figure 7. The obtained ns-PL lifetimes $\tau_{average}$ of the samples were reduced from 11.9 ns (less than 100 K) to 7.8 ns As shown in Figure 7, $\tau_{average}$ tends to be stable (about 11.9 ns) and does not change with temperature in the low temperature range (less than 100 K), indicating that the PL lifetimes are mainly due to the radiation recombination processes of the carriers. However, the non-radiative recombination increases with increasing temperature, resulting in a continuous decrease in $\tau_{average}$, which drops to 7.8 ns at 300 K. It is worth mentioning that, the variation trend of the PL lifetimes at a certain temperature τ_{meas} (T) is consistent with the PL integration intensity of the steady-state temperature dependent PL spectra [23]. This phenomenon once again verifies the typical PL properties of luminescent N-Si-O-related defect states.

3.6 Radiative and non-radiative recombination lifetimes of a-SiN_xO_y thin films

As Section 3.5 mentioned above, we use the ns-PL lifetimes $\tau_{average}$ to determined the radiative and the non-radiative recombination lifetimes. Thus, the PL internal quantum efficiency at different temperatures (η(T)) should be determined as [5]:

$$\eta(T) = \frac{k_r(T)}{k_r(T)+k_{nr}(T)} = \frac{\frac{1}{\tau_r(T)}}{\frac{1}{\tau_r(T)}+\frac{1}{\tau_{nr}(T)}} = \frac{\tau_{average}(T)}{\tau_r(T)}, \text{with } \frac{1}{\tau_{average}(T)} = \frac{1}{\tau_r(T)} + \frac{1}{\tau_{nr}(T)}. \quad (1)$$

Here k_r(T) and k_{nr}(T) denote the radiative and the non-radiative recombination rates, and τ_r(T) and τ_{nr}(T) denote the radiative recombination lifetimes and the non-radiative recombination lifetimes. τ_r(T) and τ_{nr}(T) are expressed as [5]:

$$\tau_r(T) = \frac{\tau_{average}(T)}{\eta(T)}, \text{and } \tau_{nr}(T) = \frac{\tau_{average}(T)}{1-\eta(T)} \quad (2)$$

Based on our previous work [23], we obtained the PL IQE values from TD PL spectra and the directly measured PL QYs. Thus, by combining the resulting PL IQE values with the ns-PL lifetimes, we can further determine the radiative recombination lifetimes

and non-radiative recombination lifetimes of the sample according to Equation 2. Figure 8 shows the radiative recombination lifetimes and non-radiative recombination lifetimes of a-SiN_xO_y films with different R at different detection wavelengths. The detailed of the calculated τ_r, τ_{nr}, k_r and k_{nr} by using the PL IQE (η) and the obtained lifetimes $\tau_{average}$ under room temperature for a-SiN_xO_y films with various R are listed in Table 1. We note that the trends of radiative recombination lifetimes are also consistent with the trend of the densities of the N_x defect states. When $\tau_{nr}(T)$ is much greater than $\tau_r(T)$ (R = 1, 1.5, 2.5), the radiative recombination dominates the whole recombination process, and the PL IQE is higher (~70%). When $\tau_{nr}(T)$ is less than $\tau_r(T)$ (R = 0.3, 0.5, 5), the effect of non-radiative recombination is relatively obvious, resulting in a decrease in PL IQE (~40%).

Since the fluorescence lifetimes at low temperature are hardly affected by non-radiative recombination, we also can use that as the radiative recombination lifetimes ($\eta \sim 1$, and $\tau_{average} \sim \tau_r$ in the low temperature range) to calculate the non-radiative recombination lifetimes at room temperature. We compared the radiative and non-radiative recombination lifetimes obtained by these two different calculation methods, and obtained the similar results at last. The average τ_r is basically unchanged and tends to be stable at ~10 ns under different R conditions. These results show that the radiative recombinations of the luminescent N-Si-O defects remain in the order of 10^8 s^{-1} and keep unchanged throughout the whole recombination processes, which can be compared with those direct bandgap materials (e.g., typical cadmium selenide NCs, kr~10^8 s^{-1}).

4 Conclusion

In summary, we systematically studied the temperature dependent kinetic processes of radiative and non-radiative recombination in a-SiN_xO_y systems. We found that the PL lifetimes of a-SiN_xO_y films vary with the change of N-Si-O defect states concentrations, which is different from the typical luminescent kinetic characteristics of band tail related a-SiN_x films. By combining PL IQE values with the ns-PL lifetimes, the radiative and non-radiative recombination lifetimes of our a-SiN_xO_y systems ranged from low temperatures (~8 K) to room temperature can be determined. The radiative recombination rates were also obtained (k_r~10^8 s^{-1}), which can be compared to the results in the direct band gap.

Data availability statement

The original contributions presented in the study are included in the article/supplementary material, further inquiries can be directed to the corresponding author.

Author contributions

PZ: Writing–original draft. XL: Methodology, Writing–review and editing. LZ: Methodology, Writing–review and editing. DW: Methodology, Writing–review and editing. KW: Writing–review and editing, Software. SW: Writing–review and editing.

Funding

The author(s) declare that financial support was received for the research, authorship, and/or publication of this article. This research was funded by Jiangsu Province Industry-University-Research Cooperation Project of China (No.BY20230136), and the Open Project Foundation of the National Laboratory of Solid-State Microstructures (No. M37080).

Conflict of interest

The authors declare that the research was conducted in the absence of any commercial or financial relationships that could be construed as a potential conflict of interest.

Publisher's note

All claims expressed in this article are solely those of the authors and do not necessarily represent those of their affiliated organizations, or those of the publisher, the editors and the reviewers. Any product that may be evaluated in this article, or claim that may be made by its manufacturer, is not guaranteed or endorsed by the publisher.

References

1. Pavesi L, Negro LD, Mazzoleni C, Franzo G, Priolo F. Optical gain in silicon nanocrystals. *Nature* (2000) 408(23):440–4. doi:10.1038/35044012

2. Fadaly EM, Dijkstra A, Suckert JR, Ziss DM, Tilburg AJ, Mao CY, et al. Direct-bandgap emission from hexagonal Ge and SiGe alloys. *Nature* (2020) 580:205–9. doi:10.1038/s41586-020-2150-y

3. Joo J, Defforge T, Loni A, Kim D, Li ZY, Sailor MJ, et al. Enhanced quantum yield of photoluminescent porous silicon prepared by supercritical drying. *Appl Phys Lett* (2022) 108:153111. doi:10.1063/1.4947084

4. Basak FK, Kayahan E. White, blue and cyan luminescence from thermally oxidized porous silicon coated by green synthesized carbon nanostructures. *Opt Mater* (2022) 124:111990. doi:10.1016/j.optmat.2022.111990

5. Reyes GB, Dasog M, Na MX, Titova LV, Veinot JG, Hegmann FA. Charge transfer state emission dynamics in blue-emitting functionalized silicon nanocrystals. *Phys Chem Chem Phys* (2015) 17:30125–33. doi:10.1039/c5cp04819b

6. Dam B, Osorio CI, Hink MA, Muller R, Koenderink AF, Dohnalova K. High internal emission efficiency of silicon nanoparticles emitting in the visible range. *ACS Photon* (2018) 5:2129–36. doi:10.1021/acsphotonics.7b01624

7. Fujii M, Minami A, Sugimoto H. Precise size separation of water soluble red to near infrared luminescent silicon quantum dots by gel electrophoresis. *Nanoscale* (2020) 12:9266–71. doi:10.1039/d0nr02764b

8. Romero JJ, Arciprete ML, Rodriguez HB, Gonik E, Cacciari D, Moore AL, et al. Incorporation of N and O into the shell of silicon nanoparticles offers tunable photoluminescence for imaging uses. *ACS Appl Nano Mater* (2022) 5:8105–19. doi:10.1021/acsanm.2c01241

9. Yamada H, Watanabe J, Nemoto K, Sun HT, Shirahata N. Postproduction approach to enhance the external quantum efficiency for red light-emitting

diodes based on silicon nanocrystals. *Nanomaterials* (2022) 12:4314. doi:10.3390/nano12234314

10. Negro LD, Yi JH, Michel J, Kimerling LC, Chang TF, Sukhovatkin V, et al. Light emission efficiency and dynamics in silicon-rich silicon nitride films. *Appl Phys Lett* (2006) 88:233109. doi:10.1063/1.2208378

11. Lin KH, Liou SC, Chen WL, Wu CL, Lin GR, Chang YM. Tunable and stable UV-NIR photoluminescence from annealed SiO_x with Si nanoparticles. *Opt Express* (2013) 21(20):23416–24. doi:10.1364/oe.21.023416

12. Valenta J, Greben M, Gutsch S, Hiller D, Zacharias M. Photoluminescence performance limits of Si nanocrystals in silicon oxynitride matrices. *J Appl Phys* (2017) 122:144303. doi:10.1063/1.4999023

13. Marquez BP, Flores KE, Garcia SA, Gonzalez ZM, Moreno M, Torres A, et al. Broad and nearly white photoluminescence induced by the nitrogen incorporation in Si/SiO_xN_y multilayers. *J Lumin* (2021) 239:118397. doi:10.1016/j.jlumin.2021.118397

14. Meng L, Li S, Chen H, Lei M, Yu G, Wen P, et al. *In-situ* fabricated amorphous silicon quantum dots embedded in silicon nitride matrix: photoluminescence control and electroluminescence device fabrication. *J Lumin* (2023) 261:119913. doi:10.1016/j.jlumin.2023.119913

15. Luo Y, Yang X, Yue L, Ren DS, Chen JR. Effect of phosphorus doping on the luminescence intensity of Si-NC in SiO/Si multilayers. *Opt Express* (2023) 31(15):24566–72. doi:10.1364/oe.494438

16. Tabassum N, Nikas V, Ford B, Huang M, Kaloyeros AE, Gallis S. Time-resolved analysis of the white photoluminescence from chemically synthesized SiC_xO_y thin films and nanowires. *Appl Phys Lett* (2016) 109:043104. doi:10.1063/1.4959834

17. Coyopol A, Agustin MA, Salgado GG, Ramirez RL, Trujillo RR, Vivanco MR, et al. Effect of carbon concentration on optical and structural properties in the transition from silicon rich oxide to SiC_xO_y films formation. *J Lumin* (2022) 246:118851. doi:10.1016/j.jlumin.2022.118851

18. Wang M, Xie M, Ferraioli L, Yuan Z, Li DS, Yang DR, et al. Light emission properties and mechanism of low temperature prepared amorphous SiN_x films. I. Room-temperature band tail states photoluminescence. *J Appl Phys* (2008) 104:083504. doi:10.1063/1.2996292

19. Amosov AV, Kulchin YN, Dvurechenskii AV, Dzyuba VP. Photoluminescence and excitation energy transfer in non-stoichiometric silicon nitride. *J Lumin* (2022) 243:118615. doi:10.1016/j.jlumin.2021.118615

20. Kato H, Kashio N, Ohki Y, Seol KS, Noma T. Band-tail photoluminescence in hydrogenated amorphous silicon oxynitride and silicon nitride films. *J Appl Phys* (2003) 93:239–44. doi:10.1063/1.1529292

21. Chen KJ, Lin ZW, Zhang PZ, Huang R, Dong HP, Huang XF. Luminescence mechanism in amorphous silicon oxynitride films: band tail model or N-Si-O bond defects model. *Front Phys* (2019) 7:144. doi:10.3389/fphy.2019.00144

22. Zhang PZ, Wang SK, Chen KJ, Wu XL. Investigation on the luminescent stability in amorphous silicon oxynitride systems. *Eur Phys J Appl Phys* (2020) 89:10304. doi:10.1051/epjap/2020190258

23. Zhang PZ, Zhang L, Lyu F, Wang DB, Zhang L, Wu KP, et al. Luminescent amorphous silicon oxynitride systems: high quantum efficiencies in the visible range. *Nanomaterials* (2023) 13:1269. doi:10.3390/nano13071269

24. Xu LB, Piao H, Liu Z, Cui C, Yang DR. Sensitized electroluminescence from erbium doped silicon rich oxynitride light emitting devices. *J Lumin* (2021) 235:118009. doi:10.1016/j.jlumin.2021.118009

25. Topka KC, Diallo B, Puyo M, Papavasileiou P, Lebesgue C, Genevois C, et al. Critical level of nitrogen incorporation in silicon oxynitride films: transition of structure and properties, toward enhanced anticorrosion performance. *ACS Appl Electron Mater* (2022) 4:1741–55. doi:10.1021/acsaelm.2c00018